

# Fabrication of transparent and ultraviolet shielding composite films based on graphene oxide and cellulose acetate



Ana Carolina Mazarin de Moraes<sup>a,\*</sup>, Patricia Fernanda Andrade<sup>b</sup>,  
Andreia Fonseca de Faria<sup>a,1</sup>, Mateus Batista Simões<sup>a</sup>,  
Francisco Carlos Carneiro Soares Salomão<sup>c</sup>, Eduardo Bedê Barros<sup>c</sup>,  
Maria do Carmo Gonçalves<sup>b</sup>, Oswaldo Luiz Alves<sup>a,\*</sup>

<sup>a</sup> Laboratory of Solid State Chemistry, Institute of Chemistry, University of Campinas, PO Box 6154, 13083-970 Campinas, SP, Brazil

<sup>b</sup> Institute of Chemistry, University of Campinas, PO Box 6154, 13083-970 Campinas, SP, Brazil

<sup>c</sup> Department of Physics, Federal University of Ceará, PO Box 6030, 60455-900 Fortaleza, CE, Brazil

## ARTICLE INFO

### Article history:

Received 4 November 2014

Received in revised form 7 January 2015

Accepted 22 January 2015

Available online 31 January 2015

### Keywords:

Cellulose acetate

Graphene oxide

Composite films

Ultraviolet shielding

## ABSTRACT

Graphene oxide (GO) has been considered a promising filler material for building polymeric nanocomposites because of its excellent dispersibility and high surface area. In this work, we present the fabrication and characterization of transparent and ultraviolet (UV) shielding composite films based on GO and cellulose acetate (CA). GO sheets were found to be well-dispersed throughout the CA matrix, providing smooth and homogeneous composite films. Moreover, the GO sheets were completely embedded within the CA matrix and no presence of this nanomaterial was found at the surface. Nevertheless, CAGO composite films offered an improved high energy light-shielding capacity when compared to pristine CA films. Particularly for UVC irradiation, the CAGO film containing 0.50 wt% GO displayed a UV-shielding capacity of 57%, combined with 79% optical transparency under visible light. These CAGO composite films can be potentially applied as transparent UV-protective coatings for packing biomedical, pharmaceutical, and food products.

© 2015 Elsevier Ltd. All rights reserved.

## 1. Introduction

Graphene is a one-atom thick  $sp^2$ -bonded carbon arranged in a honeycomb lattice that has emerged as a novel two-dimensional material, opening up a range of possibilities for new applications (Geim & Novoselov, 2007; Novoselov et al., 2004). The extent of  $\pi$ -conjugation in graphene yields outstanding physical properties (Allen, Tung, & Kaner, 2010) such as high mobility of charge carriers, quantum Hall effect at room temperature, tunable band gap, high thermal conductivity, high elasticity, excellent optical transmittance, and large specific surface area (Dreyer, Todd, & Bielawski, 2014; Rao, Sood, Subrahmanyam, & Govindaraj, 2009; Verdejo, Bernal, Romasanta, & Lopez-Manchado, 2011). The production of high quality and defect-free graphene is time-consuming and low-throughput. As a consequence, chemically derived graphene,

especially graphene oxide (GO), has arisen to overcome these drawbacks associated with the production of graphene-based materials. GO possesses the basal plane and edges of the sheets functionalized with oxygen-containing groups (epoxy, carboxyl, carbonyl, and hydroxyl), resulting in a strongly hydrophilic and highly reactive material (Park & Ruoff, 2009; Soldano, Mahmood, & Dujardin, 2010).

Graphene-based materials have potential applicability as sensors, paper-like materials, photovoltaic devices, drug delivery systems, and polymer composites (Dreyer, Park, Bielawski, & Ruoff, 2010). In particular, GO presents promising features, capable of improving polymer properties such as elastic modulus, tensile strength, and thermal stability (Young, Kinloch, Gong, & Novoselov, 2012; Zhu et al., 2010). For instance, thin films of poly(lactic acid) and graphene oxide (PLA/GO) prepared by solvent-casting presented increased mechanical property and higher barrier to gases (Pinto, Cabral, Tanaka, Mendes, & Magalhaes, 2013). Moreover, chitosan films modified with GO showed ductile properties and excellent optical transparency (Pan, Wu, Bao, & Li, 2011). The incorporation of GO to polyimide allowed the preparation of transparent composite films highly impermeable to moisture (Tseng, Liao, Chiang, & Tsai, 2012).

\* Corresponding authors. Tel.: +55 19 3521 3394; fax: +55 19 3521 3023.

E-mail addresses: [anacmmo@gmail.com](mailto:anacmmo@gmail.com), [anacarmaz@yahoo.com.br](mailto:anacarmaz@yahoo.com.br) (A.C.M. de Moraes), [oalves@iqm.unicamp.br](mailto:oalves@iqm.unicamp.br) (O.L. Alves).

<sup>1</sup> Current address: Department of Chemical and Environmental Engineering, Yale University, New Haven, CT 06520, USA.

Indeed, the presence of oxygenated functional groups enables a good interaction and compatibility between GO and a wide range of polymers. Additionally, these chemical groups improve the dispersion of GO in aqueous media or organic polar solvents, thus facilitating the preparation of polymer nanocomposites *via* solvent-casting (Verdejo et al., 2011; Young et al., 2012).

Cellulose acetate (CA) is a thermoplastic biodegradable polymer produced primarily through the esterification of renewable and naturally abundant cellulosic materials such as cotton, wood, sugarcane, and recycled paper (Fischer et al., 2008). Owing to excellent optical transparency and electronic insulation, CA-based nanocomposites find applications as packing films, plastic devices, filters, membranes, adhesives, coatings for papers, and electrical isolation devices (Edgar et al., 2001). In addition, oxidized carbon nanotubes and graphene oxide have been blended to CA matrix in order to prepare composite materials with interesting properties. Li, Kim, and Jeong (2010) prepared acid-treated multiwalled carbon nanotube (COOH-MWCNT)/CA nanocomposites *via* the melt-compounding method. The incorporation of COOH-MWCNT led to composites with enhanced thermal stability compared to those prepared from non-oxidized MWCNT. The improvement in thermal properties is related to specific interactions between carboxyl groups in COOH-MWCNT and ester groups of CA. Gopiraman, Fujimori, Zeeshan, Kim, and Kim (2013) prepared cellulose acetate-based nanofibers through electrospinning. The incorporation of graphene containing COOH groups improved the brittleness of the hybrid fibers, which showed a Young modulus that was 3.7 fold higher than pure CA nanofibers. Last, graphene flakes incorporated into CA matrix favored the reduction of bubble defects and increased the tensile strength of nanocomposites by 31.8% compared to the non-modified films (Liu et al., 2014).

Among the several physicochemical properties of polymeric nanocomposites, the barrier against ultraviolet (UV) light enables very special applications. Specifically, overexposure to UV radiation may damage human health, and also induce DNA mutation in skin cells, causing photosensitive dermatoses or skin cancer (Sinha & Hader, 2002). UV light can also destroy covalent bonds in organic materials, causing a series of undesirable degradation effects in polymers, woods, dyes, pigments, and semiconductor devices (Andrady, Hamid, & Torikai, 2003). Generally, UV radiation absorption results in free radicals that induce chemical reactions and subsequent photodegradation (Nowicki, Richter, Wolf, & Kaczmarek, 2003). As a result, most polymers experience a reduction in their properties when exposed to UV light. In this context, many efforts have addressed the development of transparent polymeric films with UV-shielding properties, including applications such as protective UV coatings and optical filters (Calvo, Smirnov, & Miguez, 2012; Tu et al., 2010). Typically, metal oxide nanoparticles such as TiO<sub>2</sub>, ZnO, ZnS, and CeO<sub>2</sub> have been blended to polymers allowing the preparation of hybrid nanocomposites with UV-shielding capacity (Zhang, Zhuang, Xu, & Hu, 2013). These nanoparticles have been applied as UV-absorbing materials because of their low cost, good stability, and low toxicity. However, because of their photocatalytic activity, these nanomaterials can induce polymer photodegradation as a side-effect (Calvo et al., 2012).

In contrast to metal oxide nanoparticles, GO is a non-catalytic, transparent towards visible light, and a good UV light absorbing material. Furthermore, due to its large surface area and high aspect ratio, the improvements in properties of polymer nanocomposites can be achieved using low concentrations of GO (Zhu et al., 2010).

In this study, we propose the fabrication and characterization of novel and alternative composite films prepared from graphene

oxide and cellulose acetate through solvent-casting. The incorporation of GO to the CA matrix resulted in transparent films with enhanced UV-shielding properties. These composite films can be used in applications such as UV-protective agents for food, pharmaceutical, biomedical, and electronic products.

## 2. Experimental

### 2.1. Materials and chemicals

Natural graphite powder (98.0%) was purchased from Synth (Brazil) and used without any prior purification. Potassium permanganate (KMnO<sub>4</sub>, 99.0%), sulfuric acid (H<sub>2</sub>SO<sub>4</sub>, 95.0–98.0%), hydrochloric acid (HCl, 36.5–38.0%), hydrogen peroxide (H<sub>2</sub>O<sub>2</sub>, 30.0%), and acetone (99.5%) were also obtained from Synth. Sodium hydroxide (NaOH, >99.0%, pellets) was obtained from Merck, tetrahydrofuran (THF, GPC grade, 99.9%) from Scharlau, and ethanol (99.5%, P. A.) from Neon (Brazil). Phosphorous pentoxide (P<sub>2</sub>O<sub>5</sub>, 98.0%), potassium persulfate (K<sub>2</sub>S<sub>2</sub>O<sub>8</sub>, 99.0%), and cellulose acetate (CAS number 9004-35-7,  $M_n = 30,000 \text{ g mol}^{-1}$ ) were provided by Sigma-Aldrich and used as received. Deionized (DI) water was supplied from a Milli-Q® water purification system. All chemicals were analytical grade.

### 2.2. Preparation and characterization of graphene oxide (GO)

Single layered GO sheets were synthesized by the modified Hummers method (Hummers & Offeman, 1958; Tung, Allen, Yang, & Kaner, 2009). Briefly, graphite was pretreated to ensure complete oxidation. Natural graphite powder (1 g) was placed into an 80 °C solution of concentrated H<sub>2</sub>SO<sub>4</sub> (4.4 mL), K<sub>2</sub>S<sub>2</sub>O<sub>8</sub> (0.8 g) and P<sub>2</sub>O<sub>5</sub> (0.8 g). The dark blue mixture was kept on a hotplate under magnetic stirring for 4.5 h. Shortly after, heating was stopped and the mixture was diluted with DI water (170 mL) and left overnight. On the following day, the mixture was filtered using a 0.22 µm PVDF (polyvinylidene fluoride) membrane (Millipore®) and washed with DI water until the filtrate reached neutral pH. The dark isolated solid was dried in air overnight at room temperature.

For the oxidation procedure, the pretreated graphite was added slowly into a chilled flask at 0 °C containing concentrated H<sub>2</sub>SO<sub>4</sub> (40 mL). KMnO<sub>4</sub> (5 g) was gradually added over 15–20 min and the temperature was controlled to not exceed 10 °C. The ice bath was removed and the resultant dark brown-purple mixture was allowed to react at 35 °C for 2 h. DI water (77 mL) was then added in small aliquots, and an ice bath was used to maintain the temperature below 50 °C. After the water addition, the mixture was kept stirring for an additional 2 h. At that point, more DI water (230 mL) was introduced into the flask. Immediately after, 30% H<sub>2</sub>O<sub>2</sub> (4 mL) was added resulting in a bright-yellow mixture that was allowed to settle for 2 days. The mixture was decanted and the clear supernatant was removed. The remaining mixture was purified by centrifugation and washing with 10% HCl (500 mL) followed by DI water to remove metal ions and acid, respectively. The product was suspended in DI water to give a stable viscous brown dispersion, which was dialyzed for 10 days to remove residual salts (Fisherbrand dialysis tubing 12,000–14,000 Da). The resulting homogeneous graphite oxide dispersion was lyophilized and stored in a sealed vessel. GO suspensions were obtained by dispersing the product in polar solvent followed by sonication in an ultrasound bath (Cole-Parmer 8891).

GO functional groups were identified by Fourier transform infrared spectroscopy (FTIR) and X-ray photoelectron spectroscopy (XPS). FTIR spectrum was performed in a Bomem MB B100 spectrometer in the 400–4000 cm<sup>-1</sup> wave number range through a sample prepared using a homogeneous potassium bromide (KBr)

pellet. XPS spectra were obtained using a VG Thermo alpha 110 hemispherical analyzer and an AlK $\alpha$  X-ray source.

The morphology of GO sheets was observed by transmission electron microscopy (TEM) using a Zeiss LIBRA 120 microscope coupled to an Omega Filter-spectrometer with an accelerating voltage of 120 kV. The sample was prepared by dropping a 100  $\mu\text{g mL}^{-1}$  GO dispersion onto a lacey carbon grid (300 mesh).

The crystallographic structure was analyzed by X-ray diffraction (XRD) using a Shimadzu XRD-700 diffractometer. Analysis was conducted with CuK $\alpha$  X-ray radiation ( $\lambda = 1.54056 \text{ \AA}$ ) with a generator voltage of 40 kV in a  $2\theta$  range from  $5^\circ$  to  $50^\circ$  with a scan rate of  $2^\circ \text{ min}^{-1}$ .

The thermal behavior of GO was investigated through thermogravimetric analysis (TGA) using a thermogravimetric analyzer (TA Instruments SDTQ600). The temperature range employed was from 25 to  $800^\circ\text{C}$  with a ramp of  $10^\circ\text{C min}^{-1}$  under a synthetic air flow rate of  $100 \text{ mL min}^{-1}$ .

### 2.3. Characterization of cellulose acetate (CA)

As cellulose acetate (CA) was commercially obtained, the characterization to determine its real degree of polymerization (DP) and substitution (DS) was carried out. The CA number- and weight-average molecular weights ( $M_n$  and  $M_w$ , respectively) were determined by gel permeation chromatography (GPC) using a Viscotek GPCmax VE 2001 instrument with a Viscotek VE 3580 refractive index detector. The analysis was made in THF at  $40^\circ\text{C}$ , at a  $1.0 \text{ mL min}^{-1}$  flow rate. A  $5.0 \text{ mg mL}^{-1}$  CA solution concentration and  $100 \mu\text{L}$  injection volume was used. The obtained molar masses were related to polystyrene standards ( $1050$  to  $3800,000 \text{ g mol}^{-1}$ ). The average molecular weights for CA were  $M_n = 41,600 \text{ g mol}^{-1}$  and  $M_w = 97,300 \text{ g mol}^{-1}$ , and the DP value was 170.

The CA degree of substitution (DS) is the average number of acetyl groups per anhydro-D-glucose unit of cellulose (Puleo, Paul, & Kelley, 1989). DS was determined by saponification of the ester and titration of the free acid, as described by Rodrigues et al. (2008). To do this,  $2.50 \text{ mL}$  acetone was added to an Erlenmeyer flask containing about  $0.1 \text{ g}$  CA to maximize the polymer solubilization. Furthermore,  $2.50 \text{ mL}$  ethanol followed by  $5.00 \text{ mL}$  NaOH ( $0.25 \text{ mol L}^{-1}$ ) were added to the previous CA solution. After  $48 \text{ h}$  exposure,  $10.00 \text{ mL}$  HCl ( $0.25 \text{ mol L}^{-1}$ ) was added to the mixture, which was left standing for  $2 \text{ h}$ . Next, the mixture was titrated using a standard  $0.24 \text{ mol L}^{-1}$  NaOH solution, and phenolphthalein as an indicator.

The percentage of acetyl groups (%AG) was calculated by the following equation:

$$\%AG = \frac{[(V_{b_i} + V_{b_t})\mu_b - (V_a \times \mu_a)]43 \times 100}{m_{CA}},$$

where  $V_{b_i}$  corresponds to the NaOH volume added to the system;  $V_{b_t}$  is the NaOH volume used in titration;  $\mu_b$  and  $\mu_a$  are the NaOH and HCl concentrations;  $V_a$  is the HCl volume added to the system; 43 is the molar weight of the acetyl group; and  $m_{CA}$  is the mass of the cellulose acetate sample.

The degree of substitution (DS) was obtained according to Samios, Dart, and Dawkins (1997) by the following equation:

$$DS = \frac{3.86 \times \%AG}{102.4 - \%AG}.$$

The DS value was found to be  $2.37 \pm 0.09$  (39.0% of AG) for CA, which characterizes the commercial product as a cellulose diacetate.

### 2.4. Fabrication and characterization of cellulose acetate and graphene oxide (CAGO) composite films

CA was dried in a vacuum at  $60^\circ\text{C}$  for  $24 \text{ h}$  prior to use. The polymeric solution was prepared by dissolving CA ( $1.5 \text{ g}$ ) in acetone ( $7 \text{ mL}$ ) by continuous magnetic stirring for  $12 \text{ h}$ . The desired amount of GO ( $1.5$ ;  $3.75$ ; and  $7.5 \text{ mg}$ ) was dispersed in acetone ( $4 \text{ mL}$ ) and subjected to sonication in an ultrasound bath (Cole-Parmer 8891) for  $30 \text{ min}$ . Subsequently, the GO suspension in acetone was slowly added dropwise into the CA solution under gently controlled magnetic stirring to avoid bubbling. The mixture was kept stirring for  $15 \text{ min}$  under sealed conditions at room temperature to obtain a homogeneous dispersion.

Next, the CAGO composite films were prepared by solvent-casting. The mixture was spread onto a glass plate and left to dry at room temperature to allow the acetone to evaporate totally and give films that were approximately  $20 \mu\text{m}$  thick. The as-prepared films were immersed in DI water to detach them from the glass plate and then allowed to dry at room temperature for  $12 \text{ h}$ .

The GO content in the composites were  $0.10$ ;  $0.25$ ; and  $0.50 \text{ wt\%}$  in relation to CA weight, resulting in CAGO  $0.10\%$ ; CAGO  $0.25\%$ ; and CAGO  $0.50\%$  samples, respectively. CA films (without any GO) were prepared as a control.

FTIR spectra of CAGO films were recorded directly from the film samples on an Agilent Cary 630 FTIR spectrometer with the attenuated total reflectance (ATR) accessory.

The crystallographic structures of CAGO films were analyzed by XRD using a Shimadzu XRD-700 diffractometer. The analyses were conducted with CuK $\alpha$  X-ray radiation ( $\lambda = 1.54056 \text{ \AA}$ ) with a generator voltage of  $40 \text{ kV}$  in a  $2\theta$  range from  $5^\circ$  to  $50^\circ$  with a scan rate of  $2^\circ \text{ min}^{-1}$ .

TGA measurements of CAGO films were carried out on a thermogravimetric analyzer (TA Instruments SDTQ600). The temperature range employed was from  $25$  to  $800^\circ\text{C}$  with a ramp of  $10^\circ\text{C min}^{-1}$  under a nitrogen flow rate of  $100 \text{ mL min}^{-1}$ . The glass transition temperatures ( $T_g$ ) of composite films were determined by differential scanning calorimetry (DSC), which was performed in a DSC-Q100 calorimeter from TA Instruments. The thermal curves were obtained from  $25$  to  $300^\circ\text{C}$  at a  $10^\circ\text{C min}^{-1}$  scanning rate and under an argon flow of  $50 \text{ mL min}^{-1}$ .

The surface morphologies of the CAGO films were observed by SEM, in a JEOL JMS 6360-LV microscope. Samples were gold sputtered in a Bal-Tec MD 020 instrument (Balzers).

The dispersion and morphology of GO in the CA matrix were observed by TEM using a Zeiss LIBRA 120 microscope coupled to an Omega Filter-spectrometer with an accelerating voltage of  $80 \text{ kV}$ . Ultrathin sections, approximately  $40$ – $65 \text{ nm}$  thickness, were cut perpendicular to the film plane at room temperature using a diamond knife (Diatome) on a Leica EM FC6 ultramicrotome and collected on uncoated  $400$  mesh copper grids.

AFM tapping mode imaging and Kelvin probe force microscopy (KPFM) of CA and CAGO films were taken on a Nanoscope Multimode III (Veeco) employing MESP (Bruker) Co–Cr coated cantilevers ( $2.8 \text{ N/m}$  force constant,  $75 \text{ kHz}$  nominal resonance frequency).

The wettability of film surfaces was estimated by water drop contact angle measurements. After dropping  $5 \mu\text{L}$  of ultrapure water onto a film surface, the contact angle between water and the film surface was collected automatically using a KRÜSS EasyDrop drop shape analyzer instrument.

Ultraviolet-visible (UV–vis) spectroscopy was performed to study the effect of GO sheets on the UV–vis transmittance of CAGO films. For each sample, wavelength scanning was performed in three random places along the film. The wavelength was monitored



from 200 to 800 nm, and spectra were taken on an Agilent/Varian Cary 50 UV–vis spectrophotometer.

### 3. Results and discussion

Graphene oxide sheets were synthesized by the modified Hummers method. FTIR spectrum reveals the peak intensities of GO oxygen-containing groups (Fig. 1(A)). GO shows a broad and intense band ranging from 3050 to 3750  $\text{cm}^{-1}$  assigned to the presence of hydroxyl stretching vibrations in alcohols (C–OH), carboxylic acid (C(O)OH) and  $\text{H}_2\text{O}$ . More precisely, O–H stretching mode appeared at approximately 3425  $\text{cm}^{-1}$ . C–H stretching modes were identified through small bands in the range of 2850 to 2920  $\text{cm}^{-1}$ . Carbonyl (C=O) groups are revealed at 1735  $\text{cm}^{-1}$ . The peak found at 1626  $\text{cm}^{-1}$  is assigned to in-plane vibrations of  $\text{sp}^2$ -hybridized carbon atoms (C=C). Stretching modes of C–OH, C–O–C, and C–O are assigned to 1390, 1222, and 1053  $\text{cm}^{-1}$ , respectively. The bands at lower frequencies can be associated with epoxide, hydroxyl, carboxyl, and ketone groups (Faria et al., 2012; Krishnamoorthy, Veerapandian, Yun, & Kim, 2013; Wang, Shi, Yu, Chen, Zhu, & Hu, 2012).

XPS analysis was employed to quantitatively elucidate the chemical nature of GO. The C/O atomic ratio for GO was calculated as 2.9 from a survey XPS scan (Fig. 1(B)). The high-resolution C1s spectrum of GO (Fig. 1(C)) shows the components that correspond to different functional groups: epoxy, hydroxyl, carboxyl, and non-oxygenated C ring. Spectral deconvolution curves indicate four profile peaks assigned to C=C  $\text{sp}^2$  (284.5 eV), C–C  $\text{sp}^3$  (285.1 eV), C–O (286.4 eV), and C=O (288.5 eV). The  $\text{Csp}^2/\text{Csp}^3$  ratio was found to be 3.5, corroborating with the results demonstrated by Shao et al. (2012). These results are in agreement with FTIR characterization and confirm the presence of oxygenated groups on GO sheets, which is consistent with the strong hydrophilic nature of this carbon-based nanomaterial (Stankovich et al., 2007; Wang et al., 2012).

Typical tapping mode AFM image of GO (Fig. 2(A)) revealed sheets with average thicknesses of 1.15 nm (Fig. 2(B)) and lateral dimensions of micrometers, suggesting the complete exfoliation of GO into monolayers or few-layers material. GO sheets are supposed to be thicker than a flat pristine graphene sheet due to the presence of oxygenated groups on both sides of the layer (Pan et al., 2011; Stankovich et al., 2006). It is worth mentioning that the topography can also be affected by residual solvent and mica surface roughness (Liu et al., 2014). Additionally, TEM image (Fig. 2(C)) unveiled the transparent and smooth surface of the GO sheets. Furthermore, the GO sheets were found to be very stable under the electron beam (Faria et al., 2012).

XRD patterns show the crystalline features of precursor graphite, GO, CA, and CAGO composite films (Fig. 3(A)). The typical diffraction peak of pristine graphite at  $2\theta = 26.6^\circ$  indicates an interlayer spacing of 0.33 nm between (002) atomic planes in graphite (Zhang et al., 2009). After the oxidation procedure, the diffraction peak was shifted to  $2\theta = 10.46^\circ$ , providing evidence that GO is greatly different from the precursor graphite (Shao et al., 2012). This (002) diffraction peak for raw GO yields an interlayer spacing value of 0.84 nm, and the incremental distance is attributed to the introduction of oxygen moieties onto the GO surface. All of these oxygenated groups were incorporated on GO structure during the chemical oxidation of graphite.

To identify the ordered structure of GO in the cellulose acetate nanocomposites, the XRD patterns of CA and CAGO films were analyzed, and the results are shown in Fig. 3(A). Regardless of the GO content in the CAGO films, it was not possible to identify diffraction peaks associated with the ordered structure of GO. This indicates that the GO sheets are well dispersed and exfoliated throughout the

CA matrix, without the formation of ordered graphitic aggregates (Jeon, An, & Jeong, 2012).

ATR-FTIR spectra of CA and CAGO films are shown in Fig. 3(B), and no appreciable differences were observed between the spectrums of pure CA and CAGO films. All films presented a broad band at 3475  $\text{cm}^{-1}$  and a band at approximately 1734  $\text{cm}^{-1}$ , which are assigned to hydroxyl (O–H) and carbonyl (C=O) stretching of cellulose acetate, respectively (de Oliveira, Ferrarezi, Yoshida, & Goncalves, 2012). The vibrational modes at 1434  $\text{cm}^{-1}$  and 1366  $\text{cm}^{-1}$  are attributed to  $\text{CH}_2$  bending and C–H deformations of the carbon chain of cellulose acetate, respectively. An intense band at 1216  $\text{cm}^{-1}$  is assigned to C–O stretching of acetyl groups, and the band at 1161  $\text{cm}^{-1}$  is attributed to C–O–C bridge antisymmetric stretching. The symmetric stretching of the C–O bond from primary alcohol is identified at 1026  $\text{cm}^{-1}$ , and the band at 896  $\text{cm}^{-1}$  can be ascribed to  $\beta$  glucosidic linkages between sugar units that form the polymeric chain of cellulose acetate (Barud et al., 2008). Considering that ATR technique collects information from the film surface, and no significant differences were observed between the FTIR spectra of CA and CAGO films, we do believe that the chemical surface composition of the composite films was not affected by the incorporation of GO.

TGA analysis of GO is presented in Fig. 3(C). The curve displays two typical steps of thermal decomposition. The first weight loss ( $\sim 28\%$ ), between 180 and 210  $^\circ\text{C}$ , can be ascribed to the decomposition of oxygen-moieties. The abrupt mass loss of  $\sim 47\%$  observed in the range of 498–517  $^\circ\text{C}$  can be attributed to the decomposition of graphitic regions (de Faria et al., 2014).

Accordingly, the thermal stability of CA and CAGO films are also shown in Fig. 3(C). The TGA curves showed a one-step profile of weight loss for neat CA and CAGO composites, which is related to the degradation of acetyl groups and the chains of cellulose (de Oliveira et al., 2012). Therefore, it is clearly seen that the TGA curves of pure CA and CAGO films are practically overlapped, indicating that the thermal decomposition behavior of CAGO is almost identical to neat CA films, even for the highest GO loading. As aforementioned, the oxygenated groups in GO decomposed at approximately 200  $^\circ\text{C}$ ; however, the decomposition temperature of the CAGO film was approximately 350  $^\circ\text{C}$ , which suggests a strong interaction between GO sheets and CA chains. A one-step thermal decomposition of chitosan/GO films was also observed by Han, Yan, Chen, and Li (2011).

Quantitatively, the incorporation of GO into the CA matrix slightly improved the thermal stability of the composite films, as evaluated from the thermal degradation temperatures at 10% and 50% weight losses ( $T_{10\%}$  and  $T_{50\%}$ ) (Table 1). For example, the thermo-oxidative degradation values at 10% and 50% of neat CA film were 312.7 and 349.7  $^\circ\text{C}$ , respectively, whereas  $T_{10\%}$  and  $T_{50\%}$  of CAGO 0.50% were 317.9 and 359.0  $^\circ\text{C}$ , respectively, which are slightly higher than the values for neat CA. Likewise, the thermal stability of CA/graphene flakes composites was also slightly improved after modification with graphene, as demonstrated by Liu et al. (2014).

The glass transition temperatures ( $T_g$ ) for neat CA, CAGO 0.10%, CAGO 0.25%, and CAGO 0.50% films were 189.1  $^\circ\text{C}$ , 190.5  $^\circ\text{C}$ , 190.1  $^\circ\text{C}$ , and 174.0  $^\circ\text{C}$ , respectively (Table 1). The relatively high CA  $T_g$  value is reported to be the result of the formation of complex molecular associates, which depend on the strength and amount of intra and intermolecular interactions between CA chains. These interactions between the cellulose chain units are responsible for making CA structure particularly rigid. The  $T_g$  of the CAGO 0.50% film (174.0  $^\circ\text{C}$ ) was lower than the  $T_g$  value of pure CA film (189.1  $^\circ\text{C}$ ). This decrease is attributed to the segmental motion enhancement of the polymer backbone and indicates that the addition of GO sheets restricts CA associate formation, consequently decreasing the  $T_g$  value of the CA matrix (Romero, Leite, & Goncalves, 2009).

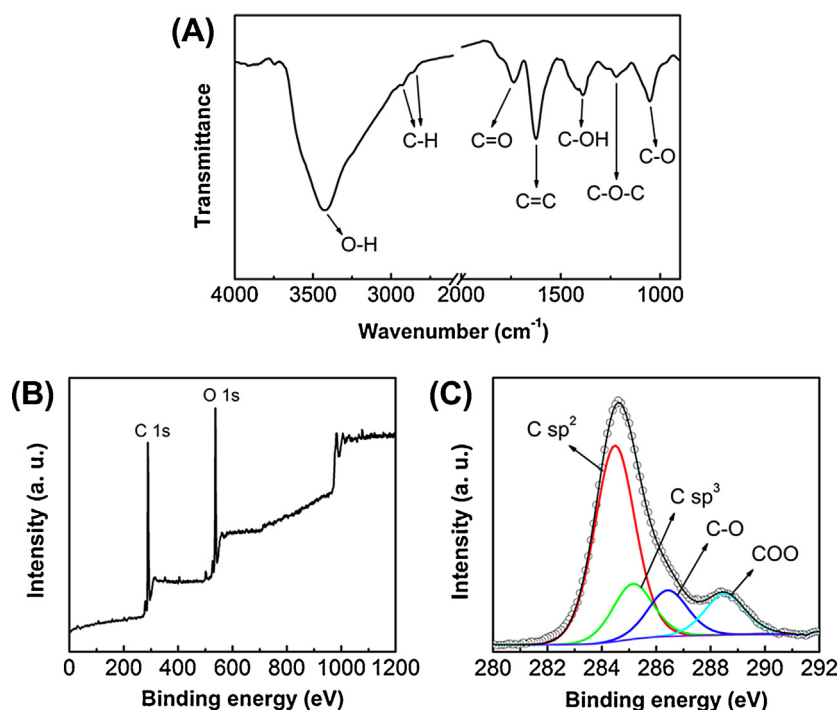


Fig. 1. (A) FTIR spectrum of graphene oxide. (B) Survey XPS scan of GO. (C) High-resolution XPS scan for C1s of GO.

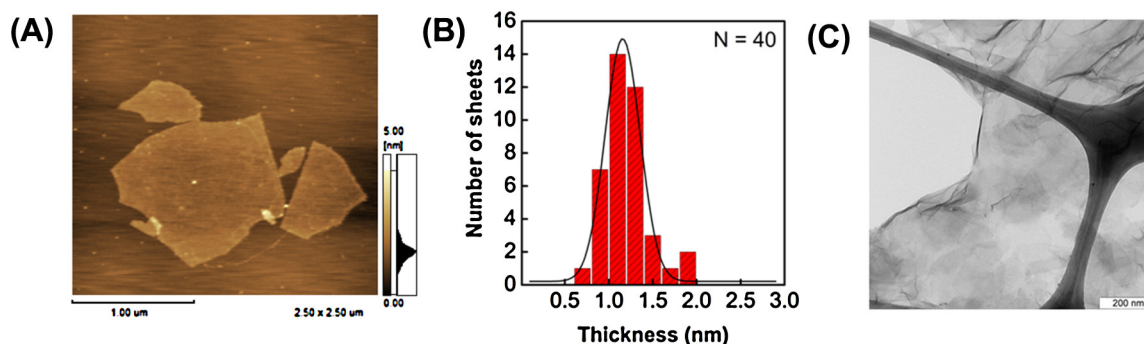


Fig. 2. (A) Tapping mode AFM image of GO. (B) Histogram of height of GO sheets ( $N=40$ ). (C) TEM image of GO sheet.

The melting temperature ( $T_m$ ) for neat CA film was found to be 221.8 °C, which is in agreement with values previously reported in the literature (Braganca & Rosa, 2003; Fidale et al., 2010). The  $T_m$  remained practically unaltered with the incorporation of 0.10 and 0.25 wt% GO; however, no melting transition was observed for the CAGO 0.50% film.

The melting enthalpy ( $\Delta H_m$ ) for neat CA film was found to be 2.77 J g<sup>-1</sup>, and the incorporation of GO into the films did not show appreciable differences in this value. The  $\Delta H_m$  value indicates the amorphous nature of the films, which is very small compared to the melting enthalpy of 58.8 J g<sup>-1</sup> calculated for a

perfect cellulose acetate crystal (Cerqueira, Rodrigues, & Assuncao, 2006).

The morphological properties of CA and CAGO films were characterized by SEM, as shown in Fig. 4(A)–(D)). The SEM image of pure CA film (Fig. 4(A)) displays a highly smooth film surface, and the SEM images of CAGO samples (Fig. 4(B)–(D)) showed that the incorporation of GO did not provide significant morphological changes to the surface roughness; CAGO film surfaces were also homogeneous and smooth. Nevertheless, smoothness observed in the SEM images is an indication of the fact that the GO sheets were uniformly dispersed in the CA matrix, exhibiting films with high

Table 1

Thermal degradation temperatures for 10% and 50% weight losses ( $T_{10\%}$  and  $T_{50\%}$ ) of CA and CAGO films. Glass transition temperatures ( $T_g$ ), melting temperatures ( $T_m$ ) and melting enthalpies ( $\Delta H_m$ ) of the films. Average contact angles measured by water droplet on CA and CAGO film surfaces. The numbers in parentheses represent the standard deviation for  $n=3$ .

Samples	TGA		DSC			Contact angle (°)
	$T_{10\%}$ (°C)	$T_{50\%}$ (°C)	$T_g$ (°C)	$T_m$ (°C)	$\Delta H_m$ (J g <sup>-1</sup> )	
CA	312.7	349.7	189.1	221.8	2.77	71.4 (1.3)
CAGO 0.10%	318.0	348.1	190.5	222.4	2.86	71.2 (1.1)
CAGO 0.25%	317.5	348.8	190.1	220.6	2.30	71.4 (1.7)
CAGO 0.50%	317.9	359.0	174.0	–	–	69.7 (1.6)

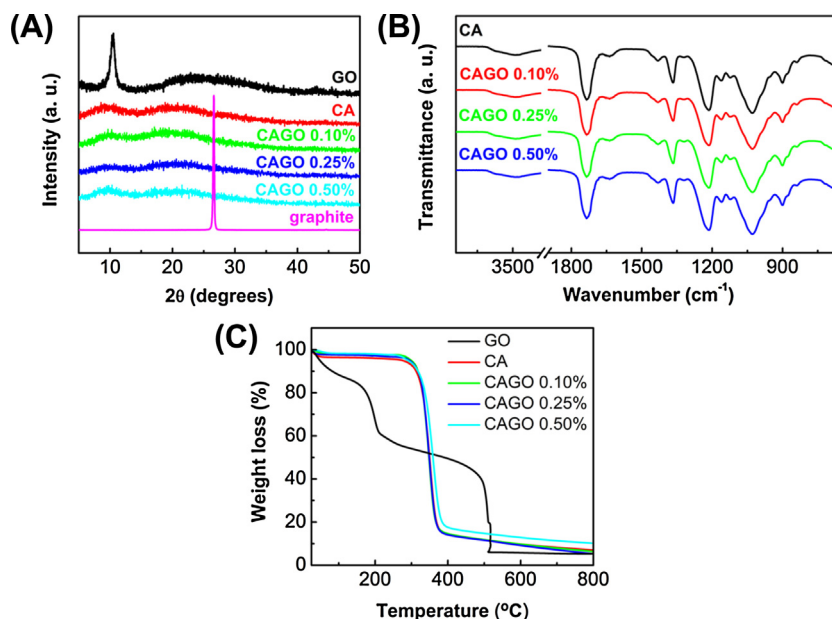


**Fig. 3.** (A) XRD patterns of raw GO, CA, and CAGO composite films (CAGO 0.10%, CAGO 0.25%, and CAGO 0.50%). (B) FTIR spectra of CA and CAGO composite films recorded with attenuated total reflectance (ATR) accessory. (C) TGA plots for raw-GO, CA, and CAGO composite films.

homogeneity without visible points of aggregation. Therefore, the GO oxygenated groups might be interacting with the CA chains, providing good compatibility between the GO filler and the polymer.

TEM analysis was carried out to investigate the dispersion of GO within the CAGO composite film. The TEM images were obtained from a cross-section of the CAGO 0.50% film. As shown in Fig. 4((E)–(F)), the TEM images revealed that the GO sheets were well-distributed throughout the CA matrix, even though the GO sheets appeared to be somewhat folded within the polymeric matrix. Besides, the presence of agglomerates has not been detected. Additionally, the GO sheets were completely embedded within the polymeric matrix, indicating good adhesion between GO and the polymer chains.

For a detailed investigation of the surface morphology, height and phase images were obtained from tapping mode AFM. Fig. 5(A) shows the topographic images of CA (left) and CAGO 0.50% films (right) (scale  $5\ \mu\text{m} \times 5\ \mu\text{m}$ ). The images demonstrate that the surface of the CA film is highly homogeneous and smooth. However, some roughness was observed on the surface of the CAGO 0.50% composite film. As mentioned from previous SEM results, the incorporation of GO led to the formation of smooth film surfaces; however, AFM analysis indicates that the presence of 0.50 wt% GO in the polymeric matrix led to a film with some surface roughness, compared to the pure CA film. This roughness may be due to the presence of folded GO sheets in the polymeric matrix, as demonstrated by TEM analysis (Fig. 4((E)–(F))). As a result, the incorporation of GO was found to impart some roughness to the surface of CAGO composite films without considerably reducing their homogeneity and smoothness features.

Phase imaging is a technique commonly employed to study the phase contrast (material contrast) of polymeric blends and composites. Fig. 5(B) displays the phase image of CA (left) and CAGO 0.50% films (right). The CA contrast image is homogeneous. The phase imaging of CAGO 0.50% film identified more clearly the surface roughness as compared to its corresponding height image (Fig. 5(A) right). Hence, the surface homogeneity is maintained after the incorporation of GO into the CA matrix, and no specific regions where GO sheets are present were distinguishable.

KFPM measurements were taken to obtain the electrostatic potential maps for CA and CAGO 0.50% films. Fig. 5(C) (left) and its corresponding electrostatic surface potential curve showed no contrast and no surface potential for CA film. This behavior can be associated with the absence of superficial charge and the non-conducting nature of CA film. However, a high contrast was observed for CAGO film (Fig. 5(C) right). The corresponding electrostatic surface potential curve shows that, for some regions, the electrostatic potential was close to zero, which is equivalent to the electrostatic potential map found in pristine CA film, whereas there were some regions that showed electrostatic potentials of approximately 1 V. Therefore, the white domains, measuring from 30 to 200 nm, can be related to the presence of GO sheets dispersed throughout the entire polymeric film. These results imply that the net charge is concentrated at the areas where GO sheets are localized. It is worth mentioning that the potential value appears to be independent of the GO sheet size, indicating that the charge density at different GO sheet clusters is very similar. The KFPM results are in agreement with TEM analysis, confirming that GO is indeed dispersed across the CA matrix and that the net charge is mostly concentrated at the GO sheets. The lack of spatial correlation between the phase contrast images (Fig. 5(B)) and the KPFM measurements (Fig. 5(C)) indicates that the GO sheets are homogeneously embedded in the CA matrix and not accumulated at the surface.

To determine if the incorporation of GO altered the surface wettability, water contact angles were acquired and the results are shown in Table 1. Herein, contact angle measurements were conducted by dropping ultrapure water on pristine CA and CAGO surfaces. The incorporation of GO did not alter the hydrophilicity of CAGO films in comparison to pristine CA film. Therefore, these results strongly support that GO sheets are not directly exposed on the polymeric composite film surface, proving that the chemical compositions of the surfaces were not significantly affected by the incorporation of GO. In general, both CA and CAGO films demonstrated good wettability with water contact angles less than  $90^\circ$  (Wang, Zhang, Abidi, & Cabrales, 2009). Additionally, the wettability of CAGO 0.50% films was not substantially affected by the slight roughness of the surface, as observed from AFM imaging (Fig. 5). By contrast, Pinto et al. (2013b) found that the contact angle of PLA



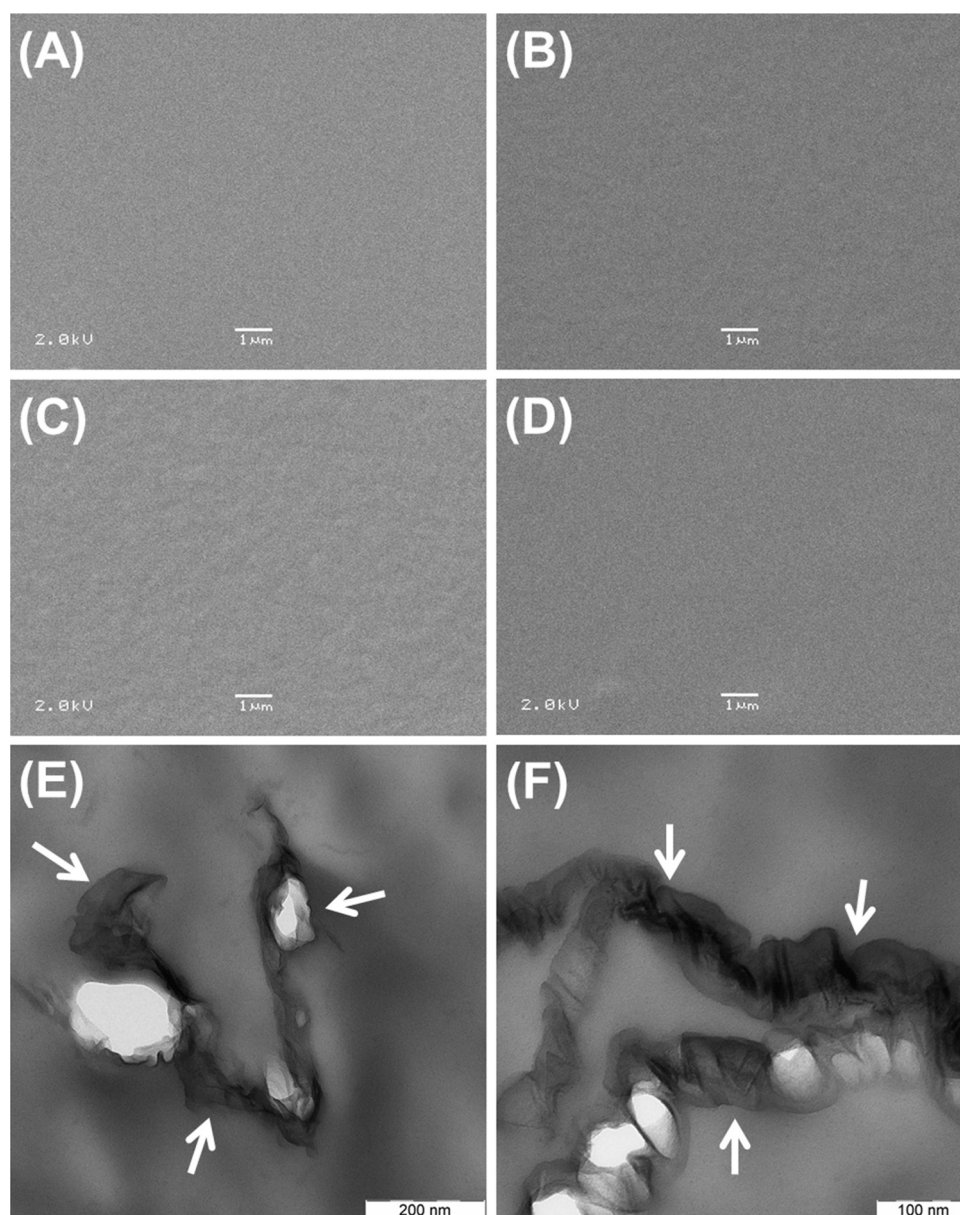


**Fig. 4.** SEM images of surfaces of (A) CA, (B) CAGO 0.10%, (C) CAGO 0.25%, and (D) CAGO 0.50%. (E–F) TEM images of CAGO film with 0.50% GO. The arrows indicate folded GO sheets.

composites decreased from  $87^\circ$  to  $78^\circ$  after blending with GO. The increase in hydrophilicity of the PLA/GO composite can be justified due to the hydrogen bonds between oxygenated-functional groups on GO and the water drop, suggesting that the GO sheets were likely exposed on the PLA/GO film surface.

Photographs of CA and CAGO films are shown in Fig. 6(A). The average thicknesses of these films were  $20\ \mu\text{m}$ . It is clear that CA is a colorless and homogeneous film, whereas the CAGO films are light-brown, and their color varies as a function of GO loading. Additionally, all CAGO composite films are visually transparent and uniform.

The light transmittance of CA and CAGO composite films was measured using UV–vis spectroscopy, and the results are shown in Fig. 6(B). Pristine CA film presented light transmittance higher than 90% across the visible light range (400–800 nm), and the transmittance of CAGO films slightly decreased with increasing GO loading. For the film containing the highest wt% GO (CAGO 0.50%), the light transmittance at 550 nm was 79%, compared to 94% for the

neat CA film. Therefore, the efficiency of visible light transmission decreased by only 15.9%. As the optical transmittance of all CAGO films within the visible range (550 nm) is still  $\sim 80$ –90%, these composite films maintained transparency regardless of GO loading. These results are in accordance with Zhang, Liu, Zheng, and Zhu (2012), who reported that cellulose films showed reduced optical transmittance (from 91.5% to 78.2%) after blending with 0.4 wt% graphene. These cellulose/graphene films revealed comparable transparency with the CA–GO films reported in the present study.

The linear decrease in light transmittance of CAGO films at 550 nm indicates that GO sheets were uniformly dispersed in the cellulose acetate matrix (Pan et al., 2011; Zhang et al., 2012). Pristine reduced graphene oxide (rGO) thin films presented optical transparency dependent on their thickness, as demonstrated by Becerril et al. (2008). Thicker rGO films (41 nm) provided transmittance of approximately 20% at 550 nm, whereas thinner films (6 nm) showed optical transparency of 95%. Although there was

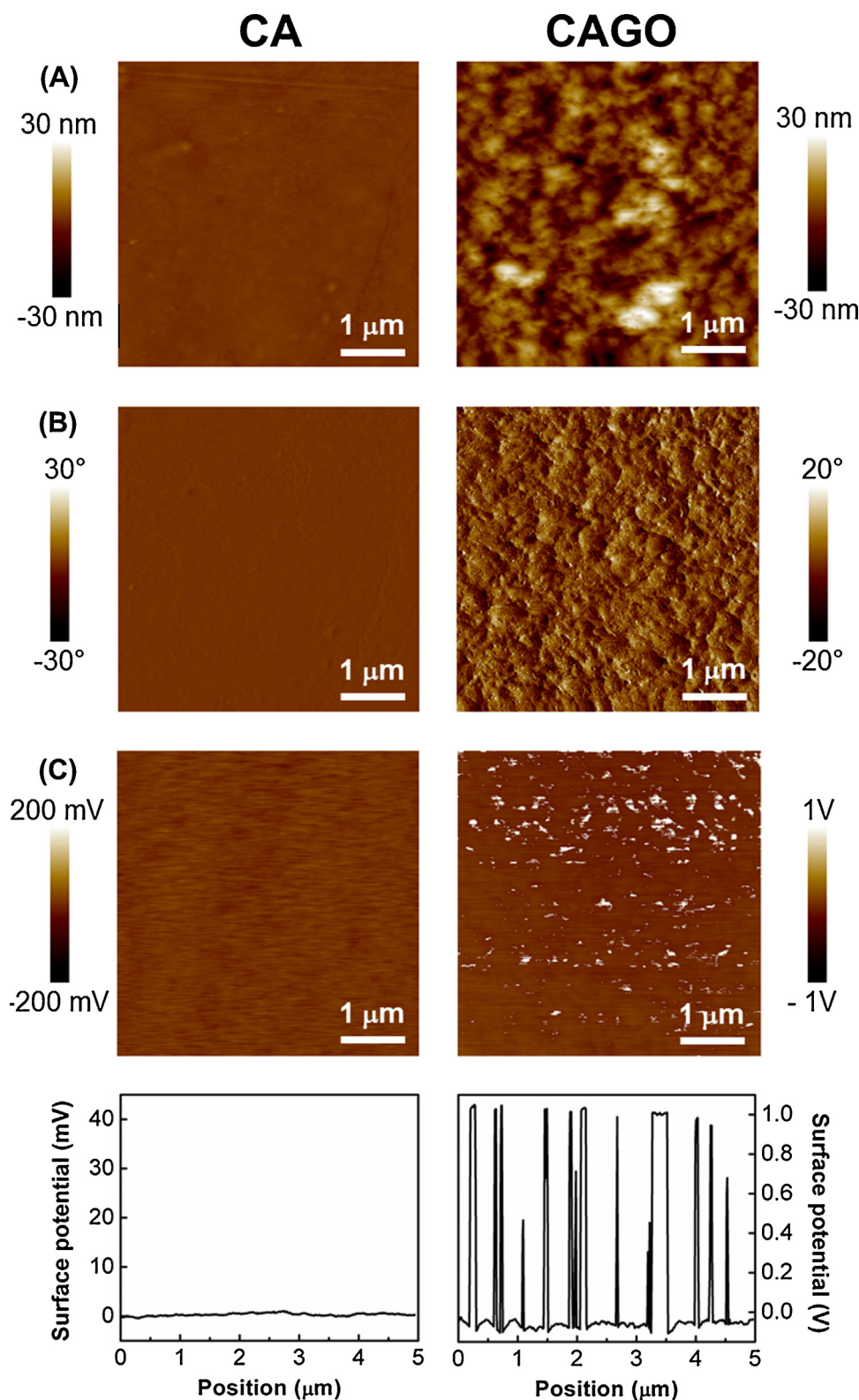


**Fig. 5.** AFM images of CA (left) and CAGO 0.50% (right) composite films (A) topography, (B) phase contrast, and (C) electrostatic surface potential.

a darkening aspect on rGO films due to the restoration of the  $\pi$ -conjugation network, a pristine thin film of GO (9 nm) was highly transparent (transmittance of 95% at 550 nm) (Becerril et al., 2008). Therefore, because CAGO films contain GO sheets distributed throughout the cellulose acetate matrix, it is reasonable to expect a slight decrease in the optical transparency for the composite films.

Fig. 6(C) shows that the transmittance changes at specific UV light wavelengths. Notably, the CAGO composite films possess good absorbance of UV light at 250 nm (UVC), 300 nm (UVB), and 350 nm (UVA), and compared to CA films, CAGO films can be considered potential UV-shielding materials. For example, CAGO 0.50% film shielded 57% UVC, 44% UVB, and 36% UVA, while neat CA film



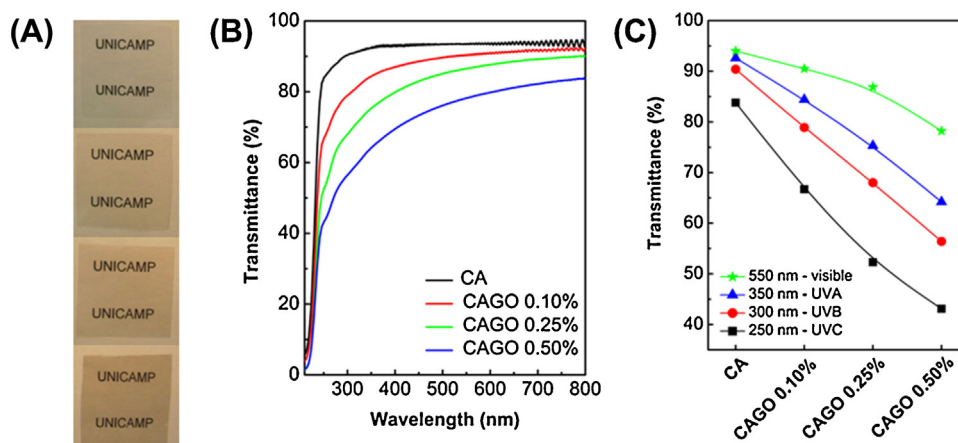


**Fig. 6.** (A) Photographs of CA and CAGO 0.10, 0.25, and 0.50% loading films, from top to bottom, respectively. (B) UV–vis spectra of neat CA and CAGO composite films. (C) Transmittance change at specific light wavelength (visible, UVA, UVB, UVC).

shielded only 16% UVC, 9.6% UVB, and 7.4% UVA. Therefore, a novel material with enhanced light shielding capacity, especially for UVC irradiation, and also good optical transparency in the visible light range was obtained through the incorporation of GO nanosheets into CA films. These results also imply that the presence of GO facilitates the absorption of UV photons (Shi et al., 2013). The schematic representation of the fabrication process of CAGO films by solvent-casting and the UV-shielding action of these transparent composite films is displayed in Fig. 7.

In this work, we were interested in the application of non-functionalized GO as a filler nanomaterial for the development

of polymeric nanocomposites with enhanced optical properties. In this context, various semiconductor metal oxide nanoparticles such as  $\text{TiO}_2$ , ZnO, ZnS, and  $\text{CeO}_2$ , have been incorporated into transparent polymers to produce functional materials with improved UV-shielding properties (Calvo et al., 2012). However, the photocatalytic activity of those nanoparticles would also induce photo-degradation of organic substances (Calvo et al., 2012), leading to undesirable side-effects. As a consequence, there is a demand for novel UV-shielding materials with higher stability and UV light absorbance ability. In this endeavor, GO is a non-catalytic material with high specific surface area that can be prepared in

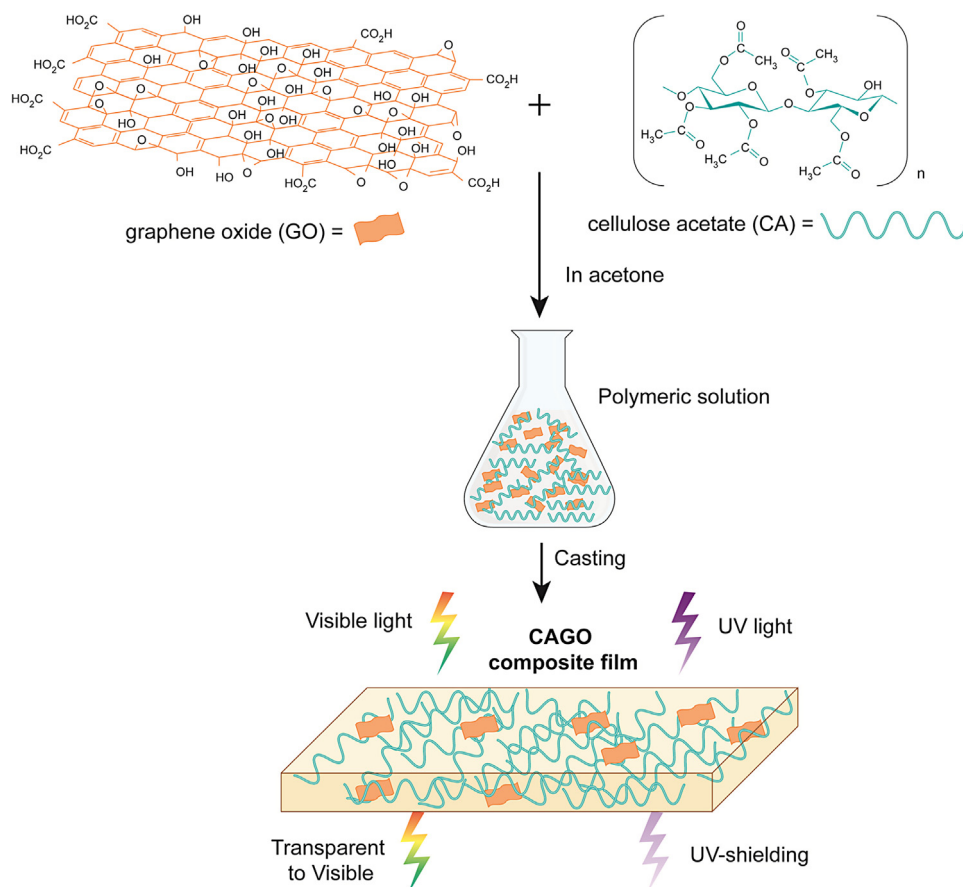


**Fig. 7.** Scheme outlining the fabrication of CAGO composite films by solvent-casting and the UV-shielding capacity of these transparent films.

large scale through the simple chemical exfoliation of natural graphite.

Furthermore, the use of GO can offer a range of advantages when compared with other nanomaterials. First, GO is a versatile material that can be functionalized by chemical and physical processes to produce nanocomposites with unique properties. Thus, the UV-shielding capacity can eventually be modulated whether GO is modified with nanoparticles or other organic molecules such as polyaromatic derivatives. In addition, GO is easily dispersible in water and organic solvents without the use of any stabilizing agent. Lastly, the oxygen-containing groups allow GO to interact with several types of polymers, thus leading to nanocomposites with new or improved properties. Nonetheless, the CAGO composite films reported in this study have potential to be applied in pharmaceutical, food, and biomedical industry as transparent coatings with strong UV light protection activity. Despite the proof of concept demonstrated in this work, additional efforts are still necessary to better understand the relationship between the physicochemical characteristics of GO materials and their UV-shielding properties in cellulose acetate films.

#### 4. Conclusions

In this study, transparent films based on graphene oxide and cellulose acetate were successfully fabricated using the solvent-casting method. Graphene oxide single sheets were found to be well-dispersed throughout the cellulose acetate matrix. The incorporation of GO did not significantly change the morphology or composition of film surfaces. The SEM and AFM micrographs proved that the CAGO film surfaces were homogeneous and smooth, and GO was not directly exposed at the composite surface. Moreover, the structural characteristics and the surface hydrophilicity of cellulose acetate films were not affected by the incorporation of GO.

The CAGO films retained the transparency in the range of 80–90% in the visible region (550 nm) regardless of GO content. However, CAGO films presented an improved UV-shielding capacity compared to pristine CA films. Particularly for UVC irradiation, CAGO 0.50% film shielded 57% of UV radiation, combined with an optical transparency in visible light of 79%. Accordingly, the incorporation of GO into CA matrix led to novel transparent films with enhanced UV light shielding capacity.

#### Acknowledgements

The authors acknowledge the financial support of São Paulo State Research Foundation (FAPESP), National Council for Technological and Scientific Development (CNPq), and National Institute of Science, Technology, and Innovation in Complex Functional Materials (INOMAT/INCT), and FUNCAP/PRONEM. The authors are also grateful to Dr. Carlos Alberto Paula Leite, Douglas Soares da Silva, and Prof. Marcelo Eduardo Huguenin Maia da Costa for their contributions to the TEM analysis, AFM imaging, and XPS analysis, respectively.

#### References

Allen, M. J., Tung, V. C., & Kaner, R. B. (2010). Honeycomb carbon: A review of graphene. *Chemical Reviews*, 110(1), 132–145.

Andrady, A. L., Hamid, H. S., & Torikai, A. (2003). Effects of climate change and UV-B on materials. *Photochemical & Photobiological Sciences*, 2(1), 68–72.

Barud, H. S., de Araujo, A. M., Santos, D. B., de Assuncao, R. M. N., Meireles, C. S., Cerqueira, D. A., et al. (2008). Thermal behavior of cellulose acetate produced from homogeneous acetylation of bacterial cellulose. *Thermochimica Acta*, 471(1–2), 61–69.

Becerril, H. A., Mao, J., Liu, Z., Stoltenberg, R. M., Bao, Z., & Chen, Y. (2008). Evaluation of solution-processed reduced graphene oxide films as transparent conductors. *ACS Nano*, 2(3), 463–470.

Braganca, F. C., & Rosa, D. S. (2003). Thermal, mechanical and morphological analysis of poly(epsilon-caprolactone), cellulose acetate and their blends. *Polymers for Advanced Technologies*, 14(10), 669–675.

Calvo, M. E., Smirnov, J. R. C., & Miguez, H. (2012). Novel approaches to flexible visible transparent hybrid films for ultraviolet protection. *Journal of Polymer Science, B—Polymer Physics*, 50(14), 945–956.

Cerqueira, D. A., Rodrigues, G., & Assuncao, R. M. N. (2006). A new value for the heat of fusion of a perfect crystal of cellulose acetate. *Polymer Bulletin*, 56(4–5), 475–484.

de Faria, A. F., de Moraes, A. C. M., Marcato, P. D., Martinez, D. S. T., Duran, N., Souza, A. G., et al. (2014). Eco-friendly decoration of graphene oxide with biogenic silver nanoparticles: Antibacterial and antibiofilm activity. *Journal of Nanoparticle Research*, 16(2), 4080–4087.

de Oliveira, A. R., Ferrarezi, M. M. F., Yoshida, I. V. P., & Goncalves, M. D. (2012). Cellulose acetate/polysilsesquioxane composites: Thermal properties and morphological characterization by electron spectroscopy imaging. *Journal of Applied Polymer Science*, 123(4), 2027–2035.

Dreyer, D. R., Park, S., Bielawski, C. W., & Ruoff, R. S. (2010). The chemistry of graphene oxide. *Chemical Society Reviews*, 39(1), 228–240.

Dreyer, D. R., Todd, A. D., & Bielawski, C. W. (2014). Harnessing the chemistry of graphene oxide. *Chemical Society Reviews*, 43, 5288–5301.

Edgar, K. J., Buchanan, C. M., Debenham, J. S., Rundquist, P. A., Seiler, B. D., Shelton, M. C., et al. (2001). Advances in cellulose ester performance and application. *Progress in Polymer Science*, 26(9), 1605–1688.

Faria, A. F., Martinez, D. S. T., Moraes, A. C. M., da Costa, M. E. H. M., Barros, E. B., Souza, A. G., et al. (2012). Unveiling the role of oxidation debris on the surface chemistry of graphene through the anchoring of Ag nanoparticles. *Chemistry of Materials*, 24(21), 4080–4087.

Fidale, L. C., Issbrucker, C., Silva, P. L., Lucheti, C. M., Heinze, T., & El Seoud, O. A. (2010). Probing the dependence of the properties of cellulose acetates and their films on the degree of biopolymer substitution: Use of solvatochromic indicators and thermal analysis. *Cellulose*, 17(5), 937–951.

Fischer, S., Thummel, K., Volkert, B., Hettrich, K., Schmidt, I., & Fischer, K. (2008). Properties and applications of cellulose acetate. *Macromolecular Symposia*, 262, 89–96.

Geim, A. K., & Novoselov, K. S. (2007). The rise of graphene. *Nature Materials*, 6(3), 183–191.

Gopiraman, M., Fujimori, K., Zeeshan, K., Kim, B. S., & Kim, I. S. (2013). Structural and mechanical properties of cellulose acetate/graphene hybrid nanofibers: Spectroscopic investigations. *Express Polymer Letters*, 7(6), 554–563.

Han, D. L., Yan, L. F., Chen, W. F., & Li, W. (2011). Preparation of chitosan/graphene oxide composite film with enhanced mechanical strength in the wet state. *Carbohydrate Polymers*, 83(2), 653–658.

Hummers, W. S., & Offeman, R. E. (1958). Preparation of graphitic oxide. *Journal of the American Chemical Society*, 80(6), 1339.

Jeon, G. W., An, J. E., & Jeong, Y. G. (2012). High performance cellulose acetate propionate composites reinforced with exfoliated graphene. *Composites, B—Engineering*, 43(8), 3412–3418.

Krishnamoorthy, K., Veerapandian, M., Yun, K., & Kim, S. J. (2013). The chemical and structural analysis of graphene oxide with different degrees of oxidation. *Carbon*, 53, 38–49.

Li, M., Kim, I.-H., & Jeong, Y. G. (2010). Cellulose acetate/multiwalled carbon nanotube nanocomposites with improved mechanical, thermal, and electrical properties. *Journal of Applied Polymer Science*, 118(4), 2475–2481.

Liu, L., Shen, Z. G., Liang, S. S., Yi, M., Zhang, X. J., & Ma, S. L. (2014). Graphene for reducing bubble defects and enhancing mechanical properties of graphene/cellulose acetate composite films. *Journal of Materials Science*, 49(1), 321–328.

Novoselov, K. S., Geim, A. K., Morozov, S. V., Jiang, D., Zhang, Y., Dubonos, S. V., et al. (2004). Electric field effect in atomically thin carbon films. *Science*, 306(5296), 666–669.

Nowicki, M., Richter, A., Wolf, B., & Kaczmarek, H. (2003). Nanoscale mechanical properties of polymers irradiated by UV. *Polymer*, 44(21), 6599–6606.

Pan, Y. Z., Wu, T. F., Bao, H. Q., & Li, L. (2011). Green fabrication of chitosan films reinforced with parallel aligned graphene oxide. *Carbohydrate Polymers*, 83(4), 1908–1915.

Park, S., & Ruoff, R. S. (2009). Chemical methods for the production of graphenes. *Nature Nanotechnology*, 4(4), 217–224.

Pinto, A. M., Cabral, J., Tanaka, D. A. P., Mendes, A. M., & Magalhaes, F. D. (2013). Effect of incorporation of graphene oxide and graphene nanoplatelets on mechanical and gas permeability properties of poly(lactic acid) films. *Polymer International*, 62(1), 33–40.

Pinto, A. M., Moreira, S., Goncalves, I. C., Gama, F. M., Mendes, A. M., & Magalhaes, F. D. (2013). Biocompatibility of poly(lactic acid) with incorporated graphene-based materials. *Colloids and Surfaces B—Biointerfaces*, 104, 229–238.

Puleo, A. C., Paul, D. R., & Kelley, S. S. (1989). The effect of degree of acetylation on gas sorption and transport behavior in cellulose-acetate. *Journal of Membrane Science*, 47(3), 301–332.

Rao, C. N. R., Sood, A. K., Subrahmanyam, K. S., & Govindaraj, A. (2009). Graphene: The new two-dimensional nanomaterial. *Angewandte Chemie—International Edition*, 48(42), 7752–7777.

Rodrigues, G., Monteiro, D. S., Meireles, C. D., de Assuncao, R. M. N., Cerqueira, D. A., Barud, H. S., et al. (2008). Synthesis and characterization of cellulose acetate produced from recycled newspaper. *Carbohydrate Polymers*, 73(1), 74–82.

Romero, R. B., Leite, C. A. P., & Goncalves, M. D. (2009). The effect of the solvent on the morphology of cellulose acetate/montmorillonite nanocomposites. *Polymer*, 50(1), 161–170.

- Samios, E., Dart, R. K., & Dawkins, J. V. (1997). Preparation, characterization and biodegradation studies on cellulose acetates with varying degrees of substitution. *Polymer*, 38(12), 3045–3054.
- Shao, G. L., Lu, Y. G., Wu, F. F., Yang, C. L., Zeng, F. L., & Wu, Q. L. (2012). Graphene oxide: The mechanisms of oxidation and exfoliation. *Journal of Materials Science*, 47(10), 4400–4409.
- Shi, W. Y., Lin, Y. J., Zhang, S. T., Tian, R., Liang, R. Z., Wei, M., et al. (2013). Study on UV-shielding mechanism of layered double hydroxide materials. *Physical Chemistry Chemical Physics*, 15(41), 18217–18222.
- Sinha, R. P., & Hader, D. P. (2002). UV-induced DNA damage and repair: A review. *Photochemical & Photobiological Sciences*, 1(4), 225–236.
- Soldano, C., Mahmood, A., & Dujardin, E. (2010). Production, properties and potential of graphene. *Carbon*, 48(8), 2127–2150.
- Stankovich, S., Dikin, D. A., Dommett, G. H. B., Kohlhaas, K. M., Zimney, E. J., Stach, E. A., et al. (2006). Graphene-based composite materials. *Nature*, 442(7100), 282–286.
- Stankovich, S., Dikin, D. A., Piner, R. D., Kohlhaas, K. A., Kleinhammes, A., Jia, Y., et al. (2007). Synthesis of graphene-based nanosheets via chemical reduction of exfoliated graphite oxide. *Carbon*, 45(7), 1558–1565.
- Tseng, I. H., Liao, Y. F., Chiang, J. C., & Tsai, M. H. (2012). Transparent polyimide/graphene oxide nanocomposite with improved moisture barrier property. *Materials Chemistry and Physics*, 136(1), 247–253.
- Tu, Y., Zhou, L., Jin, Y. Z., Gao, C., Ye, Z. Z., Yang, Y. F., et al. (2010). Transparent and flexible thin films of ZnO-polystyrene nanocomposite for UV-shielding applications. *Journal of Materials Chemistry*, 20(8), 1594–1599.
- Tung, V. C., Allen, M. J., Yang, Y., & Kaner, R. B. (2009). High-throughput solution processing of large-scale graphene. *Nature Nanotechnology*, 4(1), 25–29.
- Verdejo, R., Bernal, M. M., Romasanta, L. J., & Lopez-Manchado, M. A. (2011). Graphene filled polymer nanocomposites. *Journal of Materials Chemistry*, 21(10), 3301–3310.
- Wang, S. R., Zhang, Y., Abidi, N., & Cabrales, L. (2009). Wettability and surface free energy of graphene films. *Langmuir*, 25(18), 11078–11081.
- Wang, Y., Shi, Z. X., Yu, J. R., Chen, L., Zhu, J., & Hu, Z. M. (2012). Tailoring the characteristics of graphite oxide nanosheets for the production of high-performance poly(vinyl alcohol) composites. *Carbon*, 50(15), 5525–5536.
- Young, R. J., Kinloch, I. A., Gong, L., & Novoselov, K. S. (2012). The mechanics of graphene nanocomposites: A review. *Composites Science and Technology*, 72(12), 1459–1476.
- Zhang, L., Liang, J. J., Huang, Y., Ma, Y. F., Wang, Y., & Chen, Y. S. (2009). Size-controlled synthesis of graphene oxide sheets on a large scale using chemical exfoliation. *Carbon*, 47(14), 3365–3368.
- Zhang, X. M., Liu, X. Q., Zheng, W. G., & Zhu, J. (2012). Regenerated cellulose/graphene nanocomposite films prepared in DMAC/LiCl solution. *Carbohydrate Polymers*, 88(1), 26–30.
- Zhang, Y. W., Zhuang, S. D., Xu, X. Y., & Hu, J. G. (2013). Transparent and UV-shielding ZnO@PMMA nanocomposite films. *Optical Materials*, 36(2), 169–172.
- Zhu, Y. W., Murali, S., Cai, W. W., Li, X. S., Suk, J. W., Potts, J. R., et al. (2010). Graphene and graphene oxide: Synthesis, properties, and applications. *Advanced Materials*, 22(35), 3906–3924.